Surface Patterning

Deutsche Ausgabe: DOI: 10.1002/ange.201509356
Internationale Ausgabe: DOI: 10.1002/anie.201509356

Corrosion-Mediated Self-Assembly (CMSA): Direct Writing Towards Sculpturing of 3D Tunable Functional Nanostructures

*Jing Wang and Ghim Wei Ho**

Abstract: *Inexpensive and readily available metal foils have been extracted and sculptured into nanocomposites without the expense of applied energy. The unwanted corrosion phenomenon has been contrarily utilized to realize desirable 3D nanostructures through a corrosion-mediated self-assembly (CMSA) method, which is unattainable by conventional 2D patterning routes. By virtue of electrochemical dissolution/redeposition initiated by brass corrosion, ionic derivatives (Zn^{2+} and Cu^{2+}) are continuously supplied and seized by etchant ions (PO_4^{3-}) to self-assemble into well-defined nanocomposites. Beyond 3D geometry patterning, CMSA enables arbitrarily tailoring of structures and chemical compositions with in situ multiphase amalgamation of hybrid materials, which improves homogeneity and thus mitigates phase separation issues. Importantly, the CMSA technique is demonstrated on transition metals for functional photocatalytic applications.*

Compared to patterned 2D nanomaterials, 3D nanomaterials offer large surface areas with unique optical, electrical, and physicochemical features that are attractive in view of practical applications.[1,2] Specifically, fabricating patterned 3D nanostructures of such dimensional scale, complexity, and material diversity require high degree of control and laborious processes.[3] Furthermore, most conventional nanofabrication methods are only adapted for 2D patterning of finite thickness that limits their applications,[4] while layer-by-layer stacking of 2D patterns to create 3D nanostructures poses significant challenges in alignment and planarization processes.[5]

Corrosion is a commonly observed phenomenon where destruction of materials (usually metals) are initiated by chemical reactions with their environment.[6] It refers to a process where metal is eroded by etchants, which results in dissolution into constituent ions, ultimately forming their respective oxides or inorganic salts.[7] Contrarily, corrosion of metals under specific conditions can be utilized to bring about desirable architectures.[8–20] Following this, extending corrosion-mediated self-assembly (CMSA) to 3D geometry patterning, without considering chemical, resist, or developer incompatibilities as well as substrate flatness and alignment issues,[21,22] is attractive yet unexplored approach towards unique nanosculpturing that can be readily exploited on a large scale. In contrast to naturally occurring corrosion, there are some fundamental differences in the CMSA process. In general, metal corrosion by exposing to the environment or immersing in etchants is usually uncontrollable and time-consuming.[23] On the contrary, directly dispensing of controlled etchants onto a predefined material surface may shorten the corrosion process. More importantly, it is feasible for a straightforward and selective area-sculpturing of materials towards 3D functional nanostructures, which is comparable to the "pen-on-paper" creation of flexible printed electronics and fluorescent patterns.[24,25] Other than demonstrating on a variety of transition metals, direct corrosion of an alloyed material facilitates amalgamation of multiphase nanocomposites at the atomic level, which improves material homogeneity and deters phase separation. Such fulfilment will invariably lead to enhanced physicochemical properties owing to the coupling effect of the constituent components.

Herein, we present a direct-writing process on individual zinc and copper foils as well as on brass foil, a binary alloy of copper and zinc, based on the corrosion with phosphoric acid. CMSA enables arbitrary tailoring of 3D architectures composed of zinc/copper hybrid phosphates with tunable structures and chemical compositions by manipulating acid concentrations. To the best of our knowledge, this is the first ever CMSA demonstration for direct 3D patterning and sculpturing of heterogeneous nanocomposites with structural homogeneity for functional application like photocatalysis. The hassle-free low-cost CMSA is especially motivated for large-scale 3D patterning that is less stringent in regards to high-resolution demands.

Figure 1a shows the "writing-on-metal" process with a Chinese calligraphy brush using phosphoric acid as the "ink". The letters "NUS" were written on the brass foil (Figure 1b). After drying for 12 h, a light green pattern of "NUS" emerged on the brass surface. Similarly, periodic arrays of circles with a diameter of 1 mm were achieved (Figure 1c), indicating this technique is highly versatile for direct patterning. Using SEM imaging of the letter "U" (Figure 1d,e), a clear boundary is observed between the corroded and uncorroded area. The pattern presents a well-defined 3D flower-like nanosheet architecture with a thickness of about 10 μm, while the uncorroded area remains intact, implying the localized corrosion has solely induced the formation of nanostructures. Chemical compositions and

[*] Dr. J. Wang, Prof. Dr. G. W. Ho
Department of Electrical and Computer Engineering
National University of Singapore
4 Engineering Drive 3, Singapore 117583 (Singapore)
Prof. Dr. G. W. Ho
Engineering Science Programme, National University of Singapore
9 Engineering Drive 1, Singapore 117575 (Singapore)
and
Institute of Materials Research and Engineering
A*STAR (Agency for Science, Technology and Research)
3 Research Link, Singapore 117602 (Singapore)
E-mail: elehgw@nus.edu.sg

Supporting information for this article is available on the WWW under http://dx.doi.org/10.1002/anie.201509356.

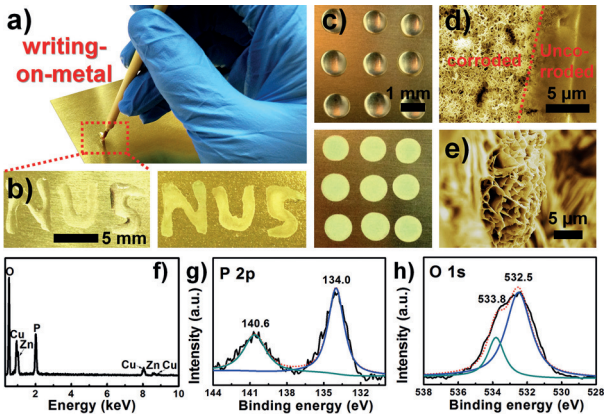

Figure 1. a) Direct writing on brass foil with phosphoric acid (1%). Optical images of b) "NUS" and (c) circle arrays before and after water evaporation. d) Top- and e) cross-sectional view SEM images, f) EDX spectrum, and g) P 2p and h) O 1s XPS spectra of the patterns.

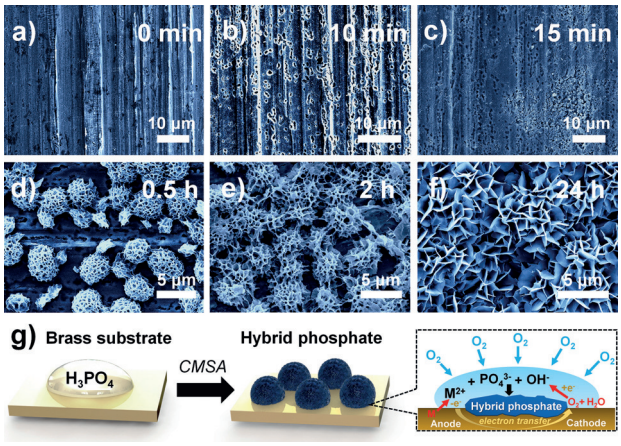

Figure 2. SEM images of brass surface at different corrosion durations: a) 0 min, b) 10 min, c) 15 min, d) 0.5 h, e) 2 h, and f) 24 h (H_3PO_4 concentration: 1%). g) Illustration of the phosphate formation.

crystalline phases of these patterns were investigated. The EDX spectrum in Figure 1 f shows the existence of only Cu, Zn, P, and O elements. In XPS spectra (Figure 1 g,h), the binding energy at 134.0 and 140.6 eV are identified as P $2p_{3/2}$ and P $2p_{1/2}$, respectively, and the peaks at 532.5 and 533.8 eV are ascribed to O 1s. The atom ratios of Cu/P and Zn/P are 1.6:1 and 1.7:1, respectively, close to that of $Cu_3(PO_4)_2$ and $Zn_3(PO_4)_2$.[10] Furthermore, an XRD spectrum (Supporting Information, Figure S1) displays several diffraction peaks that match well with zinc phosphate (JCPDS card: 29-1390) and copper phosphate (JCPDS card: 21-0298), revealing these patterns are composed of zinc/copper hybrid phosphates.

To explore the pattern formation, morphology evolution of the brass surface at different corrosion durations was recorded (Figure 2). A plain surface without micro-/nanostructures was observed before corrosion started. After corrosion for 10 min, numerous cavities with an average size of 500 nm were observed, and shortly thereafter nanoparticles of circa 200 nm with random dispersion were evidently accumulated in the vicinity of some cavities (high-magnification image in the Supporting Information, Figure S2). The brass surface was then sparsely covered with numerous isolated porous spheres (3.5 μm in size) in 30 min, along with few smaller irregular agglomerates. When corrosion was prolonged to 2 h, more spherical nanosheet structures with uniform size distribution were constructed. These structures were densely assembled into 3D architecture with flower-like ensembles after 24 h.

Metal corrosion is considered as an electrochemical dissolution/re-deposition process (Figure 2 g). Crystalline metals contain numerous dislocation defects with relatively high energy, which are easily attacked by chemical etching.[26,27] Under acidic conditions, zinc and copper atoms readily react to their ionic forms (Zn^{2+} and Cu^{2+}) from the layered brass structure at the anode (dissolution stage), as expressed in the following equations:

$$Zn \rightarrow Zn^{2+} + 2e^- \quad (1)$$

$$Cu \rightarrow Cu^{2+} + 2e^- \quad (2)$$

The generated electrons will transfer to the cathode, further reacting with oxygen from air to produce hydroxy ions:

$$O_2 + 2H_2O + 4e^- \rightarrow 4OH^- \quad (3)$$

The released Zn^{2+} and Cu^{2+} are mainly seized by PO_4^{3-} ions, coordinating into a solubilized layer of phosphate complex intermediate. Acid corrosion will perforate the intermediate, leading to selective crystallization into nanoparticles (re-deposition stage). Owing to surrounding PO_4^{3-} domains, these nanoparticles, which function as nuclei, will aggregate into larger particles, eventually self-assembling into crystal facets and shapes driven by the surface free energy.[28] As more of nanosheet spheres are produced with increasing corrosion durations, the spheres become densely packed into interconnected flower-like nanosheet network.

As reported, metal corrosion is influenced by ion concentrations, pH values, and ambient temperature.[7] In this case, the structures and chemical compositions of the hybrid phosphates are tunable by simply changing H_3PO_4 concentrations. Figure 3 shows SEM images of the phosphates synthesized at concentrations of 0.1%, 1%, and 10%. Well-defined porous spheres of about 13 μm were formed at 0.1% in the case of brass (Figure 3 a). Flower-like sheet ensembles with a wall thickness of 150 nm were observed at 1% (Figure 3 d). A further increase of concentration to 10% resulted in a radial configuration of nanowires with a diameter of 900 nm (Figure 3 g). These single entities with structural homogeneity of the hybrid phosphates exclusive of other shapes suggest that phase separation of biphasic metal components is mitigated during formation. Indeed, the structures of hybrid phosphates are similar to the sheet-like ensembles of copper phosphates at lower concentrations of 0.1% and 1% (Figure 3 b,e), but resemble nanowire architectures of zinc phosphates at higher concentration of 10% (Figure 3 i). It is also noted that weight ratios of zinc and copper in the hybrid phosphates are strikingly different. Copper content is higher than zinc at lower H_3PO_4 concen-

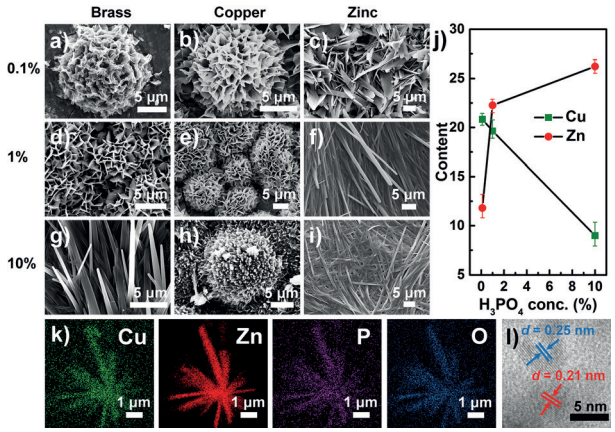

Figure 3. SEM images of a), d), g) hybrid phosphates, b), e), h) copper phosphates, and c), f), i) zinc phosphates corroded at different H_3PO_4 concentrations. j) The relationship of H_3PO_4 concentrations and zinc/copper contents. k) Elemental mapping and l) HRTEM images of hybrid phosphate nanowires (10%).

trations, but gradually decreased with the increase of acid concentrations. A reverse trend is found in the zinc content, which increases as acid concentration is raised (Figure 3j). The corrosion process of the alloyed system is complicated, and several parameters, such as the brass component, H_3PO_4 concentration, anodic potential, and the solubility product (K_{sp}), should be considered. Lower H_3PO_4 concentrations are believed to disintegrate a smaller amount of metal ions from brass, and vice versa, as indicated by Han et al., who observed that Zn^{2+} concentration increased proportionally with the etchant concentration during zinc corrosion.[29] Among these ions, Cu^{2+} exceeds Zn^{2+} in concentration owing to more copper content in brass foil. Furthermore, the K_{sp} of copper and zinc phosphates are 1.40×10^{-37} and 9.0×10^{-33}, respectively, suggesting copper phosphate is less soluble and more stable in water. Therefore, PO_4^{3-} may preferentially react with Cu^{2+} at lower acid concentrations, resulting in nanosheet structures and higher copper content in hybrid phosphates. At higher acid concentrations, however, the releasing rate of metal ions is believed to increase. In this scenario, Zn^{2+} may play the dominant role, as the anodic potentials are 0.76 V and −0.34 V for zinc and copper, respectively, implying faster generation of Zn^{2+} ions at the initial stage. Therefore, the as-obtained structure of the hybrid phosphate is closer to that of zinc phosphate with higher zinc content. Typical elemental mapping images of nanowire structures (Figure 3k) demonstrate that the elements Zn, Cu, P, and O are uniformly distributed along the nanowires. In its HRTEM image (Figure 3l), two lattice fringes with interplanar spacings of 0.25 and 0.21 nm are clearly seen, as indexed to be zinc phosphate and copper phosphate, respectively.

Sulfurization of the hybrid phosphates leads to ZnS/CuS (ZnS/CuS), forming closely interfaced heterojunctions (Supporting Information, Figures S5–S8). The hybrid sulfides, named as ZC-01, ZC-1, and ZC-10 from the corrosion concentrations, can serve as good candidates for photocatalysis that offers a promising way to solve the global energy crisis and environmental concerns.[30–37] The hydrogen generation rate of ZC-01 reached 93.1 μmol $g^{-1}h^{-1}$, which was enhanced to 152.9 μmol $g^{-1}h^{-1}$ for ZC-1 but dropped to 117.5 μmol $g^{-1}h^{-1}$ for ZC-10. These sulfides, for example, ZC-1, were able to continuously produce hydrogen at a steady rate for another four cycles (Figure 4b), indicating their stability for sustainable applications. In contrast, pure CuS

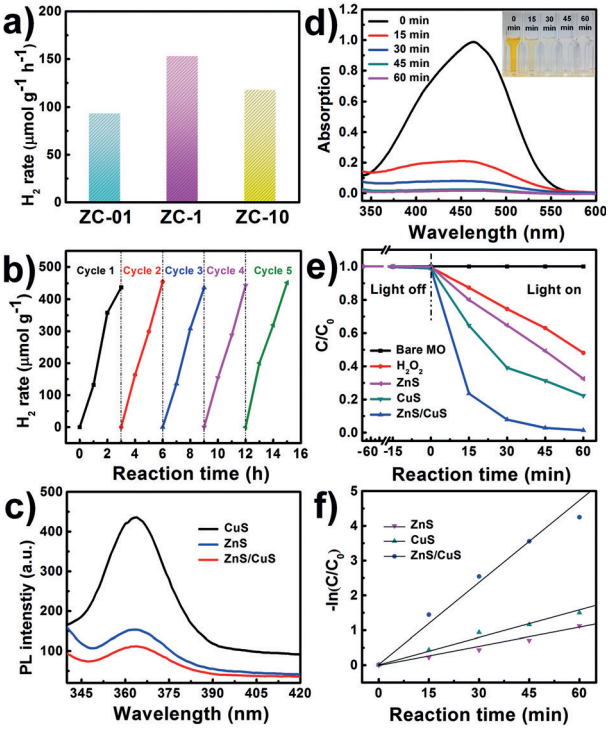

Figure 4. a) Photocatalytic H_2 production from ZnS/CuS. b) Stability test of H_2 production from ZC-1 for five cycles. c) PL emission spectra of CuS, ZnS, and ZnS/CuS ($\lambda_{ex}=300$ nm). d) UV/Vis absorption spectra and digital images of methyl orange (MO) degradation with ZC-1 at different intervals. e) Degradation kinetics and f) pseudo first-order kinetics of MO degradation in absence and presence of photocatalysts.

was incapable of producing hydrogen, while pure ZnS managed to generate hydrogen at a rate of only 33.2 μmol $g^{-1}h^{-1}$ (Supporting Information, Figure S9). Thermodynamically, the valence band edge of CuS higher than the redox potential of O_2/H_2O (1.23 eV vs NHE, pH 0) is unable to meet the requirement of bandgap alignment for photocatalytic H_2 generation.[38] The wide bandgap of ZnS (ca. 3.4 eV) primarily allows ultraviolet absorption (4–5% of the solar spectrum), giving rise to impoverished light absorption capability.[39] Therefore, it is the synergistic effect of ZnS and CuS that contributes to the enhanced photocatalysis. Generally, photocatalytic H_2 generation is dominated by the recombination of photoinduced electrons (e^-) and holes (h^+), which can be effectively explored by PL emission spectra.[40,41] As indicated in Figure 4c, CuS has a high emission at about 364 nm, while ZnS/CuS exhibited the lowest PL intensity, suggesting the e^-/h^+ recombination is greatly suppressed. The intimate heterojunctions between ZnS and CuS promote the interfacial charge transfer, where photogenerated electrons

can migrate easily from ZnS to CuS for the reduction of protons to H_2.[42] The large specific surface area from their distinct 3D structures also benefits light harvesting during water splitting.

The photocatalytic capability of ZnS/CuS was further evaluated by the photodegradation of methyl orange (MO), an often-used pollutant with mutagenic properties, with the assistance of a small amount of H_2O_2. Figure 4d shows typical UV/Vis absorption spectra of the MO solution in the presence of ZC-1 at different illumination durations. The absorption peak of MO at 462 nm rapidly decreased and eventually disappeared in 45 min. Obvious color decay from bright orange to colorless is observed at different degradation intervals of 0, 15, 30, 45, and 60 min. Under illumination, ZnS/CuS yields highly oxidative superoxide radical anions ($O_2^{\bullet-}$) and hydroxyl radicals ($OH^{\bullet}$) that will attack the azo bond in the MO molecules, eventually decomposing MO into nontoxic products.[43,44] H_2O_2 is able to produce $OH^{\bullet}$ by direct photolysis; meanwhile, it acts as an electron donor to boost the generation of $OH^{\bullet}$ from ZnS/CuS,[45] thus accelerating the degradation process. MO degradation with or without photocatalysts were performed, with their relative concentration (C/C_0) quantified by the UV/Vis absorbance (Figure 4e). The MO concentration in the absence of photocatalysts or H_2O_2 exhibited no change when illuminated for 1 h. Pure H_2O_2 without photocatalysts is able to decrease the MO concentration to 47.8%. In the cases of pure CuS and ZnS, MO concentration dropped to 22.3% and 32.5%, respectively. Consequently, ZnS/CuS completely degraded MO in 45 min, turning out to be the most effective. The kinetics of MO degradation was studied, in which the efficiency of degradation is quantitatively determined using the pseudo first-order model:

$$\ln(C_0/C_t) = kt \quad (4)$$

where C_t and C_0 are the concentration of tested and initial solution, respectively, and k is the pseudo first-order rate constant. As calculated, k was 0.0706, 0.0247, and 0.0182 min^{-1} for ZnS/CuS, CuS, and ZnS, respectively, demonstrating a superior degradation rate of hybrid sulfides.

In summary, we present for the first time a direct-writing technique by CMSA for 3D patterning of zinc/copper hybrid phosphates with tunable architectures and chemical compositions. Hybrid ZnS/CuS with well-interfaced heterojunctions were achieved by sulfurization, which produced hydrogen at a rate that was 4.6-fold higher than pure ZnS, and rapidly decomposed MO in 45 min. This CMSA approach opens up a straightforward and low-cost pathway for direct 3D patterning of nanocomposites with structural homogeneity and large surface area that is usually unachievable from 2D patterning routes. Moreover, this method is exceptionally simple and effective, in which in situ corrosion promotes multiphase integration of copper and zinc on the atomic scale, thus deterring phase separation and optimizes contact interface for enhanced heterojunction-induced charge-transfer that is beneficial for solar-energy-related applications.

Acknowledgements

This work is supported by MOE R-263-000-B38-112 and R-263-000-B63-112.

Keywords: 3D patterning · corrosion · nanocomposites · photocatalysis · self-assembly

How to cite: *Angew. Chem. Int. Ed.* **2015**, *54*, 15804–15808
Angew. Chem. **2015**, *127*, 16030–16034

[1] J.-H. Ahn, H.-S. Kim, K. J. Lee, S. Jeon, S. J. Kang, Y. Sun, R. G. Nuzzo, J. A. Rogers, *Science* **2006**, *314*, 1754–1757.
[2] K. Aoki, H. Miyazaki, H. Hirayama, K. Inoshita, T. Baba, K. Sakoda, N. Shinaya, Y. Aoyagi, *Nat. Mater.* **2003**, *2*, 117–121.
[3] Z. Chen, W. Ren, L. Gao, B. Liu, S. Pei, H.-M. Cheng, *Nat. Mater.* **2011**, *10*, 424–428.
[4] C. Faure, F. Leal-Calderon, H. Saadaoui, *Adv. Mater. Interfaces* **2014**, *1*, 1400072.
[5] S. R. Shin, B. Aghaei-Ghareh-Bolagh, X. Gao, M. Nikkhah, S. M. Jung, A. Dolatshahi-Pirouz, S. B. Kim, S. M. Kim, M. R. Dokmeci, X. Tang, A. Khademhosseini, *Adv. Funct. Mater.* **2014**, *24*, 6136–6144.
[6] F. U. Renner, A. Stierle, H. Dosch, D. M. Kolb, T.-L. Lee, J. Zegenhagen, *Nature* **2006**, *439*, 707–710.
[7] H.-D. Yu, Z. Zhang, M.-Y. Han, *Small* **2012**, *8*, 2621–2635.
[8] W. Zhang, X. Wen, S. Yang, Y. Berta, Z. L. Wang, *Adv. Mater.* **2003**, *15*, 822–825.
[9] H. Yu, D. Wang, M. Y. Han, *Adv. Mater.* **2008**, *20*, 2276–2279.
[10] X. Wu, G. Shi, S. Wang, P. Wu, *Eur. J. Inorg. Chem.* **2005**, 4775–4779.
[11] Z. Zhang, X. Shao, H. Yu, Y. Wang, M. Han, *Chem. Mater.* **2005**, *17*, 332–336.
[12] X. Wen, W. Zhang, S. Yang, *Langmuir* **2003**, *19*, 5898–5903.
[13] Z. Zhang, H. Yu, Y. Wang, M. Y. Han, *Nanotechnology* **2006**, *17*, 2994–2997.
[14] C. Lu, L. Qi, J. Yang, L. Tang, D. Zhang, J. Ma, *Chem. Commun.* **2006**, 3551–3553.
[15] J. Liu, X. Huang, Y. Li, K. M. Sulieman, X. He, F. Sun, *J. Mater. Chem.* **2006**, *16*, 4427–4434.
[16] S. Wang, L. Feng, L. Jiang, *Adv. Mater.* **2006**, *18*, 767–770.
[17] L. Li, H. Yang, H. Zhao, J. Yu, J. Ma, L. An, X. Wang, *Appl. Phys. A* **2010**, *98*, 635–641.
[18] O. Akhavan, E. Ghaderi, *J. Mater. Chem.* **2011**, *21*, 12935–12940.
[19] Y. Ding, M. Chen, J. Erlebacher, *J. Am. Chem. Soc.* **2004**, *126*, 6876–6877.
[20] H. Zhang, P. Liu, F. Li, H. Liu, Y. Wang, S. Zhang, M. Guo, H. Cheng, H. Zhao, *Chem. Eur. J.* **2011**, *17*, 5949–5957.
[21] M. J. Hynes, J. A. Maurer, *Angew. Chem. Int. Ed.* **2012**, *51*, 2151–2154; *Angew. Chem.* **2012**, *124*, 2193–2196.
[22] A. A. Eliseev, N. A. Sapoletova, I. Snigireva, A. Snigirev, K. S. Napolskii, *Angew. Chem. Int. Ed.* **2012**, *51*, 11602–11605; *Angew. Chem.* **2012**, *124*, 11770–11773.
[23] X. H. Chen, G. B. Yang, L. H. Kong, D. Dong, L. G. Yu, J. M. Chen, P. Y. Zhang, *Cryst. Growth Des.* **2009**, *9*, 2656–2661.
[24] A. Russo, B. Y. Ahn, J. J. Adams, E. B. Duoss, J. T. Bernhard, J. A. Lewis, *Adv. Mater.* **2011**, *23*, 3426–3430.
[25] J. Wang, C.-F. Wang, S. Chen, *Angew. Chem. Int. Ed.* **2012**, *51*, 9297–9301; *Angew. Chem.* **2012**, *124*, 9431–9435.
[26] B. Qian, Z. Shen, *Langmuir* **2005**, *21*, 9007–9009.
[27] G. A. El-Mahdy, *J. Appl. Electrochem.* **2005**, *35*, 347–353.
[28] H. Yan, Z. Yu, K. Lu, Y. Zhang, Z. Wei, *Small* **2011**, *7*, 3472–3478.
[29] Z. Zhang, H. Yu, X. Shao, M. Han, *Chem. Eur. J.* **2005**, *11*, 3149–3154.

[30] M. Gao, L. Zhu, W. L. Ong, J. Wang, G. W. Ho, *Catal. Sci. Technol.* **2015**, *5*, 4703 – 4726.
[31] N. Zhang, M.-Q. Yang, S. Liu, Y. Sun, Y.-J. Xu, *Chem. Rev.* **2015**, *115*, 10307 – 10377.
[32] M. Wang, L. Sun, Z. Lin, J. Cai, K. Xie, C. Lin, *Energy Environ. Sci.* **2013**, *6*, 1211 – 1220.
[33] L. Zhu, M. Hong, G. W. Ho, *Nano Energy* **2015**, *11*, 28 – 37.
[34] S. Chen, Y. Qi, T. Hisatomi, Q. Ding, T. Asai, Z. Li, S. S. K. Ma, F. Zhang, K. Domen, C. Li, *Angew. Chem. Int. Ed.* **2015**, *54*, 8498 – 8501; *Angew. Chem.* **2015**, *127*, 8618 – 8621.
[35] M. Wang, D. Zheng, M. Ye, C. Zhang, B. Xu, C. Lin, L. Sun, Z. Lin, *Small* **2015**, *11*, 1436 – 1442.
[36] Q. Kang, T. Wang, P. Li, L. Liu, K. Chang, M. Li, J. Ye, *Angew. Chem. Int. Ed.* **2015**, *54*, 841 – 845; *Angew. Chem.* **2015**, *127*, 855 – 859.
[37] Z. Lin, X. Wang, *Angew. Chem. Int. Ed.* **2013**, *52*, 1735 – 1738; *Angew. Chem.* **2013**, *125*, 1779 – 1782.
[38] J.-Y. Kim, D. Lee, H. J. Kim, I. Lim, W. I. Lee, D.-J. Jang, *J. Mater. Chem. A* **2013**, *1*, 5982 – 5988.
[39] J. Wang, Y.-F. Lim, G. W. Ho, *Nanoscale* **2014**, *6*, 9673 – 9680.
[40] Z. Shen, G. Chen, Q. Wang, Y. Yu, C. Zhou, Y. Wang, *Nanoscale* **2012**, *4*, 2010 – 2017.
[41] M. Ye, J. Gong, Y. Lai, C. Lin, Z. Lin, *J. Am. Chem. Soc.* **2012**, *134*, 15720 – 15723.
[42] T. Zhu, C. K. N. Peh, M. Hong, G. W. Ho, *Chem. Eur. J.* **2014**, *20*, 11505 – 11510.
[43] M. Ye, M. Wang, D. Zheng, N. Zhang, C. Lin, Z. Lin, *Nanoscale* **2014**, *6*, 3576 – 3584.
[44] W. Li, D. Li, Z. Chen, H. Huang, M. Sun, Y. He, X. Fu, *J. Phys. Chem. C* **2008**, *112*, 14943 – 14947.
[45] J. Liao, S. Lin, L. Zhang, N. Pan, X. Cao, J. Li, *ACS Appl. Mater. Interfaces* **2012**, *4*, 171 – 177.

Received: October 6, 2015
Published online: November 13, 2015